Advances in Nano Research, *Vol. 10, No. 3 (2021) 235-251*
DOI: https://doi.org/10.12989/anr.2021.10.3.235

Analytical solution for analyzing initial curvature effect on vibrational behavior of PM beams integrated with FGP layers based on trigonometric theories

S. Behnam Mousavi[1], Saeed Amir*[2], Akbar Jafari[1] and Ehsan Arshid[2]

[1]*Department of Mechanical Engineering, Sirjan University of Technology, Sirjan, Iran*
[2]*Department of Solid Mechanics, Faculty of Mechanical Engineering, University of Kashan, Kashan, Iran*

(*Received April 12, 2020, Revised November 23, 2020, Accepted December 18, 2020*)

Abstract. In the current study, the free vibrational behavior of a Porous Micro (PM) beam which is integrated with Functionally Graded Piezoelectric (FGP) layers with initial curvature is considered based on the two trigonometric shear deformation theories namely SSDBT and Tan-SDBT. The structure's mechanical properties are varied through its thicknesses following the given functions. The curved microbeam is exposed to electro-mechanical preload and also is rested on a Pasternak type of elastic foundation. Hamilton's principle is used to extract the motion equations and the MCST is used to capture the size effect. Navier's solution method is selected as an analytical method to solve the motion equations for a simply supported ends case and by validating the results for a simpler state with previously published works, effects of different important parameters on the behavior of the structure are considered. It is found that although increasing the porosity reduces the natural frequency, but enhancing the volume fraction of CNTs increasing it. Also, by increasing the central angle of the curved beam the vibrations of the structure increases. Designing and manufacturing more efficient smart structures such as sensors and actuators are of the aims of this study.

Keywords: curved beam; porous materials; carbon nanotubes reinforced composites; sandwich structures; trigonometric shear deformation theory; modified couple stress theory

1. Introduction

The porous medium mechanic is a branch of physics that examines the behavior of porous materials which their pores filled with a fluid such as water. The skeletal part of porous material is called matrix, which usually is solid. Porosity is the main property of the porous materials that indicates the ratio of pores volume to that of the whole. Porosity can be measured by various methods, such as observation, using an approximate microscope, gas diffusion and also using the mercury pump.

Porous materials are used in many fields of applied sciences and engineering, such as petroleum engineering, construction engineering, rock mechanics, soil mechanics and materials engineering (Liu and Chen 2014). Also, these materials are used as sound insulation due to their high strength and low weight inland transport, railways, sea and air and because of their high energy absorption capacity (Arshid and Khorshidvand 2018). Considering porosity effect in structures such as beams, plates and shells helps to gain better knowledge about their mechanical behavior.

Mechanics of porous mediums is derived from soil mechanics, in which Terzaghi, carried out specialized research in this field (Von Terzaghi 1923). He investigated a theory in which the effect of the fluid on the quasi-static deformation of the soil was accounted for. In 1935, Biot considered the mechanics of a porous material filled with fluid. His theoretical model was a solid skeleton contains pores and fluid in the pores. The concept of this model was to express that solid and fluid phases are related to each other. After Biot, the constitutive relations for porous materials were presented by Detournay and Cheng (1993). Nowadays, numerous researchers are interested in studying the mechanical behavior of porous structures. In 2004, Magnucki and Stasiewicz (2004) studied the elastic buckling of a porous beam under different loading conditions. Wattanasakulpong and Ungbhakorn (2012) studied the buckling behavior of a porous Functionally Graded (FG) beam using the Differential Quadrature Method (DQM). Bending and buckling behaviors of the FG beams presented by Chen *et al*. (2015). They used the Timoshenko beam model to account shear deformation effect and achieved the results via the Ritz method and consider the effect of different parameters on them. Ait Atmane *et al*. (2017) considered the effects of the thickness stretching and porosity on the mechanical behavior of the FG beam which was located on an elastic foundation and used Navier's method to solve the governing equations. Ebrahimi and Mokhtari (2015) presented the vibration behavior of a rotating FG porous beam and solved the equations numerically via DQM. Ebrahimi and Jafari (2016) analyzed the thermomechanical vibrations of the FG porous beam under different temperature loading using a semi-analytical differential conversion technique. Ebrahimi and Barati (2017) presented a high-order modified beam model for considering the vibration of the viscoelastic

*Corresponding author, Assistant Professor,
E-mail: Samir@kashanu.ac.ir

ISSN: 2287-237X (Print), 2287-2388 (Online)

nanocrystalline silicon nanobeam with porosity. They observed that damping frequencies of a nanocrystalline nanobeam were significantly influenced by the grain size, grain rotations, porosities, interface, damping coefficient, surface energy, nonlocality and also structural damping. Kitipornchai *et al*. (2017) researches about mechanical behavior of FG porous beam which was integrated by graphene platelets and proved that graphene platelets are very effective as the reinforcement. Arshid *et al*. (2019a) considered vibration of saturated porous plates based on classical, first-order and third-order shear deformation theories. In another work, Arshid and Khorshidvand (2018) presented the results about the effect of piezoelectric actuators on the natural frequencies of a porous plate which was integrated by piezoelectric layers. They showed the porosity increasing, reducing the natural frequency.

Composites are multi-component materials whose properties are generally better than that of each component. Each composite consists of a matrix phase and one or more reinforcement phases. Should be noted that the components of a composite do not chemically combine in such a way that these components fully maintain their chemical and natural properties and thus creating a definite common interface between the components (McEvoy and Correll 2015). Composites have several advantages, therefore they are used widely nowadays. Composite materials may be used in fuel tanks and tubes, military industries, automobile industries, marine structures, construction industry, sports equipment, medical equipment, and so on (Tayeb *et al*. 2020).

In recent years, by the rapid advancement in sciences and technologies, nanotubes are used for industrial applications (Han and Elliott 2007). In the past two decades, their usage has accelerated with the discovery of Carbon Nanotubes (CNTs) by Iijima (1991). CNTs have unique mechanical, magneto-electrical, and also chemical properties. The high rigidity and stiffness to weight ratio, electrical conductivity and high-temperature strength are among these characteristics (Ajayan and Zhou 2001). CNTs are used as reinforcement of composites and would improve their properties significantly. CNTs are divided into single-walled and multi-walled types. Single-Walled Carbon Nanotubes (SWCNTs) consist of carbon and a simple structure only. Some prediction suggests that SWCNTs can be conductive or semiconductor (Anumandla and Gibson 2006). The high electrical conductivity depends on the exact geometry of carbon atoms. SWCNTs also are divided into three major categories according to the arrangement of the carbon atoms in the tube section. Chiral and armchair, whose have a metallic property and zigzag that are semi-conductive. In zigzag and armchairs structures, the honeycomb rows in the nanotube wall are perpendicular to the nanotube axis. This structure is also called the spiral structure (Lunhui *et al*. 2008).

Mechanical analysis of Carbon Nanotubes Reinforced Composites (CNTRCs) is presented by various researchers. Thostenson and Chou (2003) modeled the elastic properties of CNTRCs in 2003. They investigated the effect of the size and structure of CNTs based on the elastic characteristics of composite base nanotubes, which was their main goal. Zhu *et al*. (2012) analyzed the static deflection and free vibration of composite plates reinforced with CNTs using the Finite Element Method (FEM) based on First-order Shear Deformation Theory (FSDT). They studied the effects of the CNTs' failure and the edge-to-thickness ratio on bending response, natural frequencies and the shape modes of the plate. The bending behavior of the composite plate reinforced by CNTs, which was located between two piezoelectric layers under a uniform mechanical load investigated by Alibeigloo (2013). Duc *et al*. (2017) considered the thermal and mechanical stability of FG CNTRC truncated conical shells. They used classical shells theory and Galerkin method to obtain the results and considered the effect of the most important variants such as semi-vertex angle and elastic medium on the linear thermal and mechanical buckling load. Lei *et al*. (2013) investigated the buckling of FG CNTRC plates. They obtained the effective properties of nanocomposite using the Eshelby-Mori-Tanaka approach and considered different parameters and their effects on the results. Critical buckling load of a quadrilateral laminated plate which was reinforced by CNTs obtained by Malekzadeh and Shojaee (2013). Their research was about the moderately thick plate and investigated the effect of material and geometrical shape parameters.

Since the behaviors of structures in macro and small dimensions are different, and also due to the application of small scale structures such as nano and microbeams, plates and shells in measuring equipment, medicine and industries, the researchers were encouraged to analyze them in small scales. One of the first studies about the mechanical behavior of the nanostructure was provided by Eringen. He presented the nonlocal theory and studied the structures in the nanoscale (Eringen 1983, 2002). After Eringen's studies, the study of small scales effects extended rapidly (Mehar and Panda 2019, Jafari and Ezzati 2017, Mirjavadi *et al*. 2020, Jafari *et al*. 2016, Benmansour *et al*. 2019, Akbas 2018). Amir *et al*. (2019) used Modified Couple Stress Theory (MCST) to capture size effect for analyzing a sandwich circular plate and a microbeam, respectively which their cores were made of porous materials.

There are different methods to solve the differential equations system for analyzing the mechanical responses of engineering structures. In this article, Navier's technique as an exact numerical method is employed which via it, the results can be extracted for simply supported boundary conditions. The main advantage of Navier's technique is its simplicity and accuracy both together. But, there are other advanced numerical methods for instance if the analytical solution could not be adopted in some problems. FEM, DQM, meshfree, finite difference, isogeometric, etc. are from the well-known ones of numerical solution methods. For example, transient responses and natural frequencies of sandwich beams with inhomogeneous FG core were investigated by Bui *et al*. (2013). They used a meshfree method to obtain the results. In another study, Bui *et al*. (2011) presented a detailed analysis of natural frequencies of laminated composite plates using the meshfree moving Kriging interpolation method. They used Kirchhoff's hypothesis for their investigation. DQM was used by Arshid *et al*. (2020a, b) to investigate two types of the microplate.

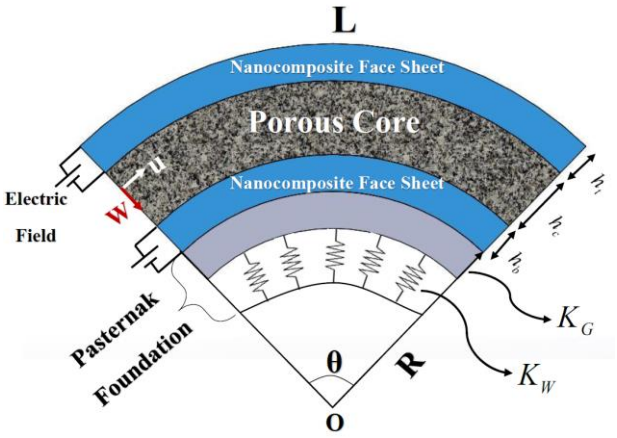

Fig. 1 Schematic diagram of the three-layered curved microbeam subjected to the electric field

The first one was three-layered, and the second one was a porous reinforced nanocomposite. The isogeometric method was used by researchers in different studies. For instance, Yu *et al*. (2019a) presented isogeometric analysis of size-dependent effects for FG microbeams by a non-classical quasi-3D theory. In another study, Liu *et al*. (2019) considered size and surface effects on the mechanical behavior of thin nanoplates incorporating microstructures using isogeometric analysis. Moreover, Fang *et al*. (2019) analyzed the mechanical behavior of porous beams by an effective computational approach based on isogeometric analysis. A novel study about size-dependent quasi-3D isogeometric beam model for two-directional FG microbeams provided by Yu *et al*. (2019b). Based on the MCST, the non-classical theory of the Reissner-Mindlin plate was extended to capture microstructure, and thus, the size effect of cracked FG microplates via an extended isogeometric analysis-based effective approach by Liu *et al*. (2018). Furthermore, a computational approach based on isogeometric analysis and a non-classical simple FSDT for size effects of FG microplates was presented by Liu *et al*. (2017).

By reviewing the literature, the authors found out that the lack of an investigation on a three-layered curved microbeam is sensible. Therefore, the main novelty of this work is its geometric type. Selection and placement of materials are other aspects of the novelties that there is no similar study in the literature like this. Taking the small-scale effects into account via the MCST integers the novelty of the current study. The main aim of the current study is to show the effect of porous and nanocomposite materials properties such as porosity, pores' distribution, central angle, CNTs' volume fraction, CNTs' distribution types, size effect and electro-mechanical preloads on vibrational behavior of the sandwich microbeam with initial curvature. Two different trigonometric shear deformation theory namely Sinusoidal Shear Deformation Beams Theory (SSDBT) and Tangential Shear Deformation Beams Theory (Tan-SDBT) are employed to describe the displacement components of the structure. Porous materials are selected as the core of the structure and its face sheets are from nanocomposites and the structure is resting on the Pasternak foundation. The mechanical properties of the three layers are varied through the thickness according to specific patterns. To the best authors' knowledge and by reviewing the literature, there is no similar research about such a structure.

2. Basic relations

2.1 Geometry

As shown in Fig. 1, the under consideration structure is a three-layered curved beam with a curvature radius of R and the central angle θ. The length of the beam is shown by L, its total thickness is shown by $H = h_c + h_t + h_b$ in which h_c, h_t, and h_b are the core, top and bottom layers' thicknesses. Noted that here, $L = R\theta$. The core of the structure is made of FG porous materials and the face sheets are from FG-CNTRCs. The mechanical properties of the three layers are varied through their thickness according to the functions which are introduced in the following. Also, the face sheets are exposed to the electric field and the beam is laid on an elastic foundation that is modeled by the Pasternak type. The Cartesian coordinate system is employed to describe the displacements of the structure which its origin is put on the left corner of the mid-surface of the beam.

2.2 Kinematic relations

The first step to analyze the above-mentioned structure is choosing the displacement field. Since accounting the shear deformation effects leads to more accurate and reliable results, so in the current study, two different higher-order trigonometric shear deformation theories namely SSDBT and Tan-SDBT are employed to describe the displacement components of the microbeam. Based on these theories, the displacement field is expressed as Ebrahimi *et al*. (2017)

$$\begin{aligned} U(x,z,t) &= u(x,t) - z\frac{\partial}{\partial x}w(x,t) + f(z)\varphi(x,t) \\ V(x,z,t) &= 0 \\ W(x,z,t) &= w(x,t) \end{aligned} \tag{1}$$

where U, V and W are the displacements of each point of the beam along the x, y and z directions, and u, v and w are those of mid-plane. Also, φ is the rotation of the middle surface around the y-axis. In the above equations, $f(z)$ is the shear deformation function which is defined for SSDBT and Tan-SDBT as follows (Ebrahimi *et al*. 2017)

$$f(z) = \frac{H}{\pi}\sin\left(\frac{\pi z}{H}\right) \qquad \text{For SSDBT} \tag{2}$$

$$\begin{aligned} f(z) &= \tan\left(\frac{\pi z}{2H}\right) r^{sec\left(\frac{\pi z}{2H}\right)}, \\ r &= 0.03 \qquad \text{For Tan} - \text{SDBT} \end{aligned} \tag{3}$$

According to Von-Karman's assumptions, the non-zero strain's components may be written as follows (Liu and

Reddy 2011).

$$\varepsilon_{xx} = \frac{\partial}{\partial x}u(x,t) - z\frac{\partial^2}{\partial x^2}w(x,t) + f(z)\frac{\partial}{\partial x}\varphi(x,t) + \frac{w(x,t)}{R}$$
$$\gamma_{xz} = \left(\frac{d}{dz}f(z)\right)\varphi(x,t) - \frac{u(x,t)}{R} + \frac{z}{R}\frac{\partial}{\partial x}w(x,t) - \frac{f(z)\varphi(x,t)}{R} \quad (4)$$

2.3 Constitutive law for the face sheets

As stated before, the face sheets of the structure are made of piezoelectric FG CNTRCs. Therefore, their constitutive relations are expressed as follows (Mohammadimehr *et al*. 2019)

$$\begin{Bmatrix}\sigma_{xx}\\ \sigma_{xz}\end{Bmatrix} = \begin{bmatrix}Q_{11}(z) & 0\\ 0 & Q_{55}(z)\end{bmatrix}\begin{Bmatrix}\varepsilon_{xx}\\ \gamma_{xz}\end{Bmatrix} - \begin{bmatrix}0 & e_{31}\\ e_{15} & 0\end{bmatrix}\begin{Bmatrix}E_x\\ E_z\end{Bmatrix} \quad (5)$$

$$\begin{Bmatrix}D_x\\ D_z\end{Bmatrix} = \begin{bmatrix}0 & e_{15}\\ e_{31} & 0\end{bmatrix}\begin{Bmatrix}\varepsilon_{xx}\\ \gamma_{xz}\end{Bmatrix} + \begin{bmatrix}0 & S_{11}\\ S_{33} & 0\end{bmatrix}\begin{Bmatrix}E_x\\ E_z\end{Bmatrix} \quad (6)$$

in which σ_{xi}, ε_{xi}, E_i and D_i (i = x, z) are the stress and strain tensors and electric field and electric displacement vectors, respectively. Also, e_{ij} and S_{ii} are piezoelectric and dielectric permeability coefficients, respectively. Furthermore, Q_{ij} are the stiffness components that are defined as follows.

$$Q_{11}(z) = \frac{E_{11}}{1-\nu^2}$$
$$Q_{55}(z) = G_{12} \quad (7)$$

In the above relations, E_{11} and G_{12} are the longitudinal Young's elasticity and the shear moduli and the Poisson's ratio is shown by ν.

There are methods to determine the effective properties of nanocomposites such as Mori-Tanaka, Halpin-Tsai and the ERM. Due to simplicity and accuracy, ERM is used to this aim in the current study. According to ERM, the longitudinal and shear moduli can be obtained using the following relations (Shen 2012)

$$E_{11} = \eta_1 E_{11CNT} V_{CNT} + V_m E_m \quad (8)$$

$$\frac{\eta_3}{G_{12}} = \frac{V_{CNT}}{G_{12CNT}} + \frac{V_m}{G_m} \quad (9)$$

where η_i (i = 1, 3) the efficiency parameters of CNTs, which is used to increase the accuracy of ERM to make the results close to experimental ones. These coefficients are obtained by molecular dynamics. Also, V_{CNT} and V_m are the CNTs and matrix volume fractions, respectively that their summation is equal to 1. Noted that the *CNT* and *m* superscripts denote those of CNTs and matrix, respectively. Other properties of nanocomposites such as density and electrical properties also follow the ERM as follows (Mohammadimehr *et al*. 2019)

$$P_{ij} = V_{CNT}P_{ij}^{CNT} + V_m P_{ij}^m \quad (10)$$

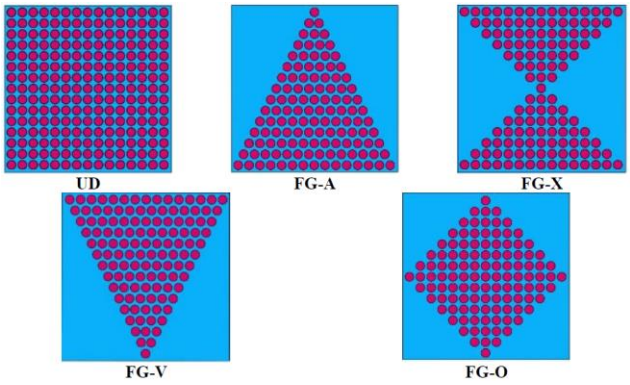

Fig. 2 Various types of CNTs distribution across the thickness of the face sheets

where P_{ij} are one of the above-mentioned properties.

Furthermore, the Poisson's ratio is determined using the following relation

$$\nu_{12} = V_{CNT}^* \nu_{12}^{CNT} + V_m \nu_m \quad (11)$$

where V_{CNT}^* is the volume fraction of CNTs which is defined as (Shen 2011).

$$V_{CNT}^* = \frac{w_{CNT}}{w_{CNT} + \left(\frac{\rho_{CNT}}{\rho_m}\right) - \left(\frac{\rho_{CNT}}{\rho_m}\right)w_{CNT}} \quad (12)$$

That w_{CNT} is the CNTs' mass fraction, ρ_{CNT} and ρ_m are CNTs and matrix density, respectively. In this study, the distribution of CNTs through the thickness direction of the face sheets is considered in five different patterns. Therefore, for the top face sheet the CNTs are distributed according to the following functions (Mohammadimehr *et al*, 2019).

$$V_{CNT}^t = V_{CNT}^* \text{UD}$$
$$V_{CNT}^t = \left[1 - \frac{2}{h_t}\left(z - \frac{h_c + h_t}{2}\right)\right]V_{CNT}^* FG\text{-}A$$
$$V_{CNT}^t = \left[1 + \frac{2}{h_t}\left(z - \frac{h_c + h_t}{2}\right)\right]V_{CNT}^* FG\text{-}V$$
$$V_{CNT}^t = 2\left[1 - \frac{2}{h_t}\left(z - \frac{h_c + h_t}{2}\right)\right]V_{CNT}^* FG\text{-}O$$
$$V_{CNT}^t = \frac{4}{h_t}\left[\left|z - \frac{h_c + h_t}{2}\right|\right]V_{CNT}^* FG\text{-}X \quad (13)$$

Also, for the bottom face sheet the CNTs distribution is considered as follow (Mohammadimehr *et al*. 2019).

$$V_{CNT}^b = V_{CNT}^* \text{UD}$$
$$V_{CNT}^b = \left[1 - \frac{2}{h_b}\left(z + \frac{h_c + h_b}{2}\right)\right]V_{CNT}^* FG\text{-}A$$
$$V_{CNT}^b = \left[1 + \frac{2}{h_b}\left(z + \frac{h_c + h_b}{2}\right)\right]V_{CNT}^* FG\text{-}V$$
$$V_{CNT}^b = 2\left[1 - \frac{2}{h_b}\left(z + \frac{h_c + h_b}{2}\right)\right]V_{CNT}^* FG\text{-}O$$
$$V_{CNT}^b = \frac{4}{h_b}\left[\left|z + \frac{h_c + h_b}{2}\right|\right]V_{CNT}^* FG\text{-}X \quad (14)$$

These patterns of CNTs distribution are shown in Fig. 2, schematically.

As stated before, the face sheets are exposed to the electric field. Noted that the electric field should be defined in such a way to satisfy Maxwell's relation. So, Arshid *et al*. (2019b) is

$$E = -\nabla\Phi \tag{15}$$

in which Φ is the electric potential function which consists of linear and cosine terms as following

$$\Phi(x,z,t) = \frac{2z}{h_f}\phi_0 - \cos\left(\frac{\pi z}{h_f}\right)\phi(x,t) \tag{16}$$

where ϕ_0 is the external applied electric potential and h_f is the thickness of the face sheets.

Substituting Eq. (16) in Eq. (15), the components of the electric field are achieved as below.

$$\begin{aligned} E_x &= -\frac{\partial\Phi}{\partial x} = \frac{\partial\phi}{\partial x}\cos\left(\frac{\pi z}{h_f}\right) \\ E_z &= -\frac{\partial\Phi}{\partial z} = -\frac{2}{h_f}\phi_0 - \frac{\pi}{h_f}\phi\sin\left(\frac{\pi z}{h_f}\right) \end{aligned} \tag{17}$$

2.4 Constitutive law for the core

The stress-strain relations for the FG porous core are demonstrated as follows

$$\begin{Bmatrix}\sigma_{xx}\\ \sigma_{xz}\end{Bmatrix} = \begin{bmatrix}A(z) & 0\\ 0 & G(z)\end{bmatrix}\begin{Bmatrix}\varepsilon_{xx}\\ \gamma_{xz}\end{Bmatrix} \tag{18}$$

where $A(z)$ and $G(z)$ are the stiffness components which are defined as

$$A(z) = \frac{E(z)}{1-\nu^2}, \qquad G(z) = \frac{E(z)}{2(1+\nu)} \tag{19}$$

In the above equations, ν is the Poisson's ratio and $E(z)$ is the elasticity Young's modulus which depends on thickness. In other words, the mechanical properties of the FG porous core are distributed across its thickness direction according to three different functions which are known as asymmetric, symmetric, and uniform porosity distributions. For each of the mentioned porosity distribution types, the following relations are ruled.

2.4.1 Non-symmetric porosity distribution

In this case, the pores are distributed non-symmetrically respect to the mid-surface of the core and the elasticity modulus and density variations are considered as following (Barati and Zenkour 2017)

$$\begin{aligned} E(z) &= E_1\left(1 - e_1\cos\left(\frac{\pi z}{2h_c} + \frac{\pi}{4}\right)\right) \\ \rho(z) &= \rho_1\left(1 - e_m\cos\left(\frac{\pi z}{2h_c} + \frac{\pi}{4}\right)\right) \end{aligned} \tag{20}$$

where e_1 is the porosity coefficient which indicated the ratio of pores to bulk volume and e_m is called the mass density coefficient of the structure which they are defined as (Arshid and Khorshidvand 2018).

$$\begin{aligned} e_1 &= 1 - \frac{G_1}{G_0} = 1 - \frac{E_1}{E_0} \\ e_m &= 1 - \frac{\rho_1}{\rho_0} = 1 - \sqrt{1-e_1} \end{aligned} \tag{21}$$

Noted that the value of e_1e1 is between zero and 1. Also, E_1 and E_0 are Young's modulus at $z = -h_c/2$ and $z = h_c/2$, ρ_1 and ρ_0 are the densities at $z = -h_c/2$ and $z = h_c/2$, respectively.

2.4.2 Symmetric porosity distribution

Unlike the previous porosity distribution, for this type of as can be expected, the pores are distributed symmetrically along with the thickness of the core. Therefore, the elasticity modulus and density are expressed as follows (Shafiei and Kazemi 2017)

$$\begin{aligned} E(z) &= E_1\left(1 - e_1\cos\left(\frac{\pi z}{h_c}\right)\right) \\ \rho(z) &= \rho_1\left(1 - e_m\cos\left(\frac{\pi z}{h_c}\right)\right) \end{aligned} \tag{22}$$

2.4.3 Uniform porosity distribution

For this type of porosity distribution, there is no dependence on z, so Panah *et al*. (2019)

$$E(z) = E_1(1-e_1), \qquad \rho(z) = \rho_1(1-e_1\chi) \tag{23}$$

where

$$\chi = \frac{1}{e_1} - \frac{1}{e_1}\left(\frac{2}{\pi}\sqrt{1-e_1} - \frac{2}{\pi} + 1\right)^2 \tag{24}$$

3. Equations derivation

3.1 Hamilton's principle

To extract the motion equations, Hamilton's principle is employed. This principle is expressed as (Berghouti *et al*. 2019)

$$\delta\int_{t_1}^{t_2}[(W_{ext} + T) - U]\,\mathrm{dt} = 0 \tag{25}$$

in which W_{ext} is the external work, U is the strain energy and T denotes the kinetic energy of curved microbeam.

As mentioned before, the current study deals with the behavior of the curved beam in small dimensions. Thus, MCST is employed to analyze the structure at the micro-scale. Based on the MCST, the strain energy can be written as following (Ghorbanpour Arani and Haghparast 2017)

$$U = \frac{1}{2}\int_V (\sigma:\varepsilon + m:\chi)\mathrm{dV} \tag{26}$$

In this relation, σ and ε are the stress and strain tensors, respectively, and m is the deviator part of the couple stress tensor and χ is the symmetric part of the curvature tensor, which they are defined as follows

$$m_{ij} = 2L_m^2 \mu \chi_{ij} \tag{27}$$

$$\chi_{ij} = \frac{1}{2}\left[\Theta_{i,j} + \Theta_{j,i}\right] \tag{28}$$

where L_m is the small scale parameter for the MCST and the Lame's coefficient is shown by μ. Also, Θ is the rotation vector which is expressed as

$$\Theta = \frac{1}{2}\nabla \times u \tag{29}$$

in which u denotes the displacement vector.

Therefore, the expanded form of the strain energy for the under consideration three-layered microbeam is written as follows.

$$\begin{aligned} U = {} & \frac{1}{2}\int_x\int_y\int_{-\frac{h_c}{2}-h_b}^{-\frac{h_c}{2}} \{\sigma_{xx}^b \varepsilon_{xx} + \sigma_{xz}^b \gamma_{xz} - D_x^b E_x - D_z^b E_z \\ & + 2m_{xy}^b \chi_{xy}^b + 2m_{yz}^b \chi_{yz}^b\} \mathrm{dV} + \frac{1}{2}\int_x\int_y\int_{-\frac{h_c}{2}}^{\frac{h_c}{2}} \{\sigma_{xx}^c \varepsilon_{xx} + \\ & + \sigma_{xz}^c \gamma_{xz} + 2m_{xy}^c \chi_{xy}^c + 2m_{yz}^c \chi_{yz}^c\} \mathrm{dV} \\ & + \frac{1}{2}\int_x\int_y\int_{\frac{h_c}{2}}^{\frac{h_c}{2}+h_t} \{\sigma_{xx}^t \varepsilon_{xx} + \sigma_{xz}^t \gamma_{xz} - D_x^t E_x - D_z^t E_z \\ & + 2m_{xy}^t \chi_{xy}^t + 2m_{yz}^t \chi_{yz}^t\} \mathrm{dV} \end{aligned} \tag{30}$$

By employing the variational calculus and integration by part, yields

$$\delta U = \int_A \left\{ \begin{array}{c} \left(-\frac{\partial}{\partial x}N_{xx} + \frac{Q_x}{R} - \frac{1}{2R}\frac{\partial}{\partial x}Y_1\right)\delta u + \left(-\frac{\partial^2}{\partial x^2}M_{xx} \right. \\ + \frac{N_{xx}}{R} + \frac{1}{R}\frac{\partial}{\partial x}R_x - \frac{\partial^2}{\partial x^2}Y_1 - \frac{1}{2R}\frac{\partial^2}{\partial x^2}Y_2 + \\ \left. + \frac{1}{2R}\frac{\partial}{\partial x}Y_5\right)\delta w + \left(-\frac{\partial}{\partial x}H_{xx} + T_x(x,t) + \frac{P_x}{R} - \right. \\ \left. \frac{1}{2}\frac{\partial}{\partial x}Y_4 - \frac{1}{2R}\frac{\partial}{\partial x}Y_3 + \frac{1}{2}Y_7 + \frac{Y_6}{2R}\right)\delta\varphi + \\ + \left(\frac{\partial}{\partial x}\bar{D}_x + \bar{D}_z\right)\delta\phi \end{array} \right\} dA \tag{31}$$

The used stress resultants are defined as follows

$$\begin{aligned} & \{N_{xx}, \quad M_{xx}, \quad H_{xx}\} = \int_z \sigma_{xx}\{1, \quad z, \quad f(z)\}\, dz \\ & \{Q_x, \quad R_x, \quad P_x, \quad T_x\} \\ & = \int_z \sigma_{xz}\left\{1, \quad z, \quad f(z), \quad \frac{d}{dz}f(z)\right\} dz \\ & \{Y_1, \quad Y_2, \quad Y_3, \quad Y_4\} \\ & = \int_z m_{xy}\left\{1, \quad z, \quad f(z), \quad \frac{d}{dz}f(z)\right\} dz \\ & \{Y_5, \quad Y_6, \quad Y_7\} = \int_z m_{yz}\left\{1, \quad \frac{d}{dz}f(z), \quad \frac{d^2}{dz^2}f(z)\right\} dz \end{aligned} \tag{32}$$

$$\begin{aligned} \bar{D}_x &= \int_z D_x \cos\left(\frac{\pi z}{h_f}\right) dz \\ \bar{D}_z &= \int_z D_z \left(\frac{\pi}{h_f}\right) \sin\left(\frac{\pi z}{h_f}\right) dz \end{aligned} \tag{32}$$

Also, the kinetic energy of the structure can be calculated as follow (Amir *et al*. 2019)

$$T = \frac{1}{2}\int_x\int_y\int_{-\frac{H}{2}}^{\frac{H}{2}} \rho(z)\left(\left(\frac{\partial U}{\partial t}\right)^2 + \left(\frac{\partial V}{\partial t}\right)^2 + \left(\frac{\partial W}{\partial t}\right)^2\right) \mathrm{dV} \tag{33}$$

And in the following it can be derived

$$\delta T = \int_A \left\{ \begin{array}{c} \left(-I_0\frac{\partial^2}{\partial t^2}u + I_1\frac{\partial^2}{\partial x \partial t^2}w - I_3\frac{\partial^2}{\partial t^2}\varphi\right)\delta u + \\ \left(I_2\frac{\partial^4}{\partial x^2 \partial t^2}w - I_1\frac{\partial^3}{\partial x \partial t^2}u - I_5\frac{\partial^3 \varphi}{\partial x \partial t^2} \right. \\ \left. -I_0\frac{\partial^2}{\partial t^2}w\right)\delta w + \left(-I_4\frac{\partial^2}{\partial t^2}\varphi + I_5\frac{\partial^3}{\partial x \partial t^2}w \right. \\ \left. -I_3\frac{\partial^2}{\partial t^2}u\right)\delta\varphi \end{array} \right\} dA \tag{34}$$

in which

$$\begin{aligned} & \{I_0, \quad I_1, \quad I_2, \quad I_3, \quad I_4, \quad I_5\} \\ & = \int_z \rho(z)\{1, \quad z, \quad z^2, \quad f(z), \quad f^2(z), \quad zf(z)\}\, dz \end{aligned} \tag{35}$$

The external work in this study consists of two parts: the first due to the elastic foundation and the second due to the mechanical and electrical preloads. So

$$W_{ext} = W_{foundation} + W_{preloads} \tag{36}$$

To determine the work of the elastic foundation, the Pasternak type is selected as a foundation. Therefore, the foundation force can be obtained via the following relation (Sobhy and Zenkour 2018)

$$f_{foundation} = K_W w(x,t) - K_G \nabla^2 w(x,t) \tag{37}$$

where K_W and K_G are the Winkler and shear layer coefficients, respectively.

Consequently, to obtain the work caused by the elastic foundation the following relation may be used (Shahsavari *et al*. 2019).

$$W_{foundation} = \frac{1}{2}\int_A \left[-f_{foundation} w(x,t)\right] \mathrm{dA} \tag{38}$$

Moreover, the work of electro-mechanical preloads can be determined using the below equation as (Amir *et al*. 2019).

$$W_{preloads} = \frac{1}{2}\int_A \left[N^{ext}\left(\frac{\partial w(x,t)}{\partial x}\right)^2\right] \mathrm{dA} \tag{39}$$

Table 1 Comparing the results for a single-layer straight macro beam with those of previously published works ($\Omega = (\omega L^2/h)\sqrt{\rho/E}$)

Ref.	Model	Ω_1	Ω_2
Pagani *et al*. (2013)	EBBT	2.859	11.535
	TBT*	2.856	11.531
	RTE**	2.859	11.552
Dan *et al*. (2016)	LP***	2.881	11.521
Ghorbanpour Arani *et al*. (2018)	EBBT	3.005	11.879
	SSDBT	2.963	11.273
Present study	EBBT	3.0071	11.8837
	SSDBT	2.9645	11.2772
	Tan-SDBT	2.9806	11.5007

* TBT: Timoshenko beams theory
** RTE: Refined Taylor expansion
*** LP: Lagrange polynomials

Here N^{ext} is the external force which includes two below parts

$$N^{ext} = N^M + N^E \tag{40}$$

where N^M denotes the mechanical preload and N^E denotes the electric preloads and are demonstrated as

$$\begin{aligned} N^M &= -P_0 \\ N^E &= -2e_{31}\phi_0 \end{aligned} \tag{41}$$

3.2 Governing equations

Finally, by substituting the Eqs. (31), (34) and (36) in Hamilton's principle and separating the coefficient of each variable, the governing equations of motion in terms of stress resultants are achieved as

$$\begin{aligned} \delta u:\ & -\frac{\partial}{\partial x}N_{xx} + \frac{Q_x}{R} - \frac{1}{2R}\frac{\partial}{\partial x}Y_1 + I_0\frac{\partial^2}{\partial t^2}u \\ & -I_1\frac{\partial^2}{\partial x\partial t^2}w + I_3\frac{\partial^2}{\partial t^2}\varphi = 0 \end{aligned} \tag{42}$$

$$\begin{aligned} \delta w:\ & -\frac{\partial^2}{\partial x^2}M_{xx} + \frac{N_{xx}}{R} + \frac{1}{R}\frac{\partial}{\partial x}R_x - \frac{\partial^2}{\partial x^2}Y_1 \\ & -\frac{1}{2R}\frac{\partial^2}{\partial x^2}Y_2 + \frac{1}{2R}\frac{\partial}{\partial x}Y_5 - K_W w + K_G\frac{\partial^2}{\partial x^2}w \\ & + N^{ext}\frac{\partial^2}{\partial x^2}w - I_2\frac{\partial^4}{\partial x^2\partial t^2}w + I_1\frac{\partial^3}{\partial x\partial t^2}u \\ & + I_5\frac{\partial^3\varphi}{\partial x\partial t^2} + I_0\frac{\partial^2}{\partial t^2}w = 0 \end{aligned} \tag{43}$$

$$\begin{aligned} \delta\varphi:\ & -\frac{\partial}{\partial x}H_{xx} + T_x + \frac{P_x}{R} - \frac{1}{2}\frac{\partial}{\partial x}Y_4 - \frac{1}{2R}\frac{\partial}{\partial x}Y_3 + \frac{1}{2}Y_7 \\ & + \frac{Y_6}{2R} + I_4\frac{\partial^2}{\partial t^2}\varphi - I_5\frac{\partial^3}{\partial x\partial t^2}w + I_3\frac{\partial^2}{\partial t^2}u = 0 \end{aligned} \tag{44}$$

$$\delta\phi:\ \frac{\partial}{\partial x}\bar{D}_x + \bar{D}_z = 0 \tag{45}$$

Table 2 Electro-mechanical properties of the matrix and reinforcement of the face sheets (Mohammadimehr *et al*. 2019)

Properties	SWCNTs	PVDF
v	0.175	0.34
ρ (kg/m^3)	1400	1780
e_{31} (C/m^2)	0	−0.13
e_{15}	0	−0.135
S_{11} (nF/m^2)	0	0.1107
S_{33}	0	0.1061
	E_{11} (TPa) = 5.6466	E_m (GPa) = 2.2
	G_{12} (TPa) = 1.9445	

4. Solution procedure

Navier's solution method is used in the current study as an analytical method to obtain the results for a simply supported ends condition curved microbeam. To this aim and to satisfy the geometrical conditions, the displacement components are considered as the below functions (Bendaho *et al*. 2019, Hadji *et al*. 2011)

$$\begin{Bmatrix} u \\ w \\ \varphi \\ \phi \end{Bmatrix} = \sum_{m=1}^{\infty} \begin{Bmatrix} U_m\cos(\alpha x) \\ W_m\sin(\alpha x) \\ \Phi_m\cos(\alpha x) \\ \Psi_m\sin(\alpha x) \end{Bmatrix} e^{i\omega t} \tag{46}$$

in which $\alpha = m\pi/L$ that m is axial wavenumber and the natural frequency is shown by ω. By replacing these functions in the governing Eqs. (42)-(45), the following matrix form can be extracted

$$([K] - \omega^2[M])\{X\} = 0 \tag{47}$$

where $\{X\}$ denotes displacements vector and the matrices $[K]$ and $[M]$ are the stiffness and mass matrices, respectively which their non-zero arrays are presented in the "Appendix" section. Solving the eigenvalue problem of Eq. (47) leads to achieving the natural frequencies of the structure.

5. Results and discussion

5.1 Validation of the results

To ensure the validity and also reliability of the equations and obtained results, and since there is no similar study to compare the results with, the natural frequencies for a simpler state are obtained and compared with those of previously published works. To this aim, natural frequencies of the two first vibrational modes of a straight macro beam are extracted. So, by tending the curvature radius of R to the infinite, neglecting the face sheets and elastic foundation, and setting the porosity coefficient and the small scale parameter of L_m to zero, the dimensionless natural frequencies are obtained and listed in Table 1 (Pagani *et al*.

Table 3 Effect of porosity coefficient on the first three natural frequencies (kHz)

Mode No.		e_1						
		0	0.1	0.2	0.3	0.4	0.5	0.6
1st	SSDBT	267.5324	265.5571	263.6130	261.7303	259.9578	258.3781	257.1408
	Tan-SDBT	268.2774	266.3304	264.4159	262.5640	260.8232	259.2763	258.0723
2nd	SSDBT	1073.1119	1064.9662	1056.9274	1049.1127	1041.7131	1035.0542	1029.7272
	Tan-SDBT	1082.3880	1074.1830	1066.0804	1058.1966	1050.7211	1043.9781	1038.5574
3rd	SSDBT	2361.6739	2343.7047	2325.9736	2308.7388	2292.4214	2277.7401	2266.0016
	Tan-SDBT	2395.4826	2377.0738	2358.8689	2341.1203	2324.2416	2308.9433	2296.5241

Table 4 Effect of porosity coefficient on the first three natural frequencies (kHz)

Porosity distribution type		e_1						
		0	0.1	0.2	0.3	0.4	0.5	0.6
Non-symmetric	SSDBT	267.5324	265.5571	263.6130	261.7303	259.9578	258.3781	257.1408
	Tan-SDBT	268.2774	266.3304	264.4159	262.5640	260.8232	259.2763	258.0723
Symmetric	SSDBT	267.5324	266.4189	265.4664	264.7354	264.3153	264.3442	265.0506
	Tan-SDBT	268.2774	267.2161	266.3214	265.6546	265.3064	265.4171	266.2178
Uniform	SSDBT	267.5324	265.3053	263.0146	260.6596	258.2424	255.7709	253.2660
	Tan-SDBT	268.2774	266.0779	263.8182	261.4983	259.1214	256.6971	254.2489

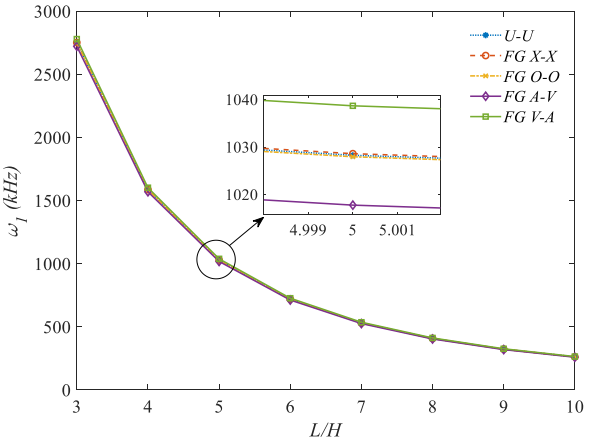

Fig. 3 Effect of CNTs distribution types on the results

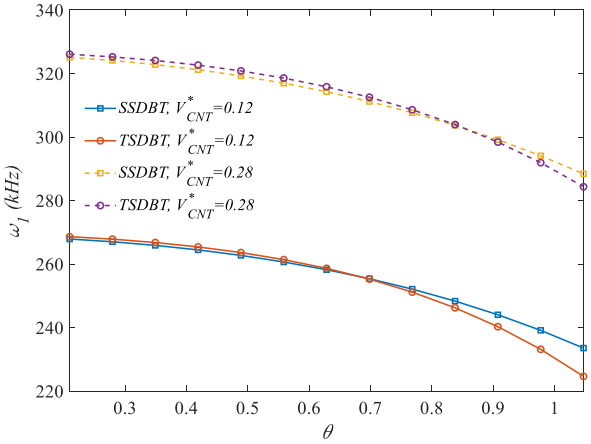

Fig. 4 Central angle variations effect on the fundamental natural frequency

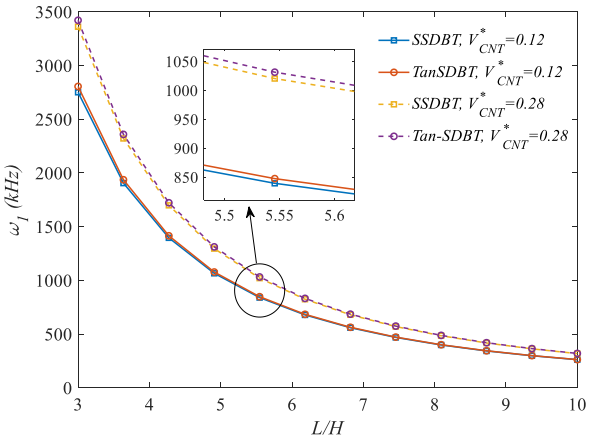

Fig. 5 Effect of CNTs volume fraction for SSDBT and Tan-SDBT

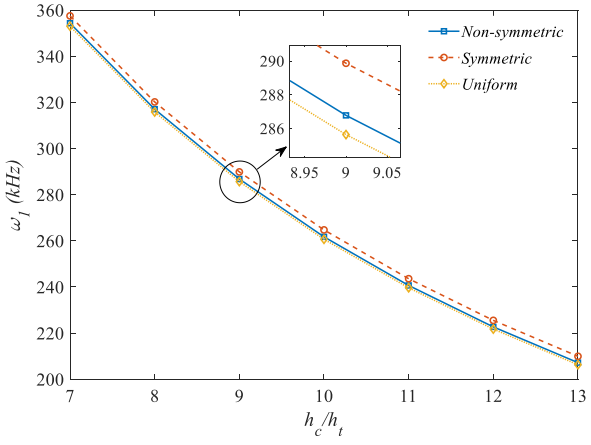

Fig. 6 Effect of layers' thicknesses and pores distribution on the fundamental natural frequency

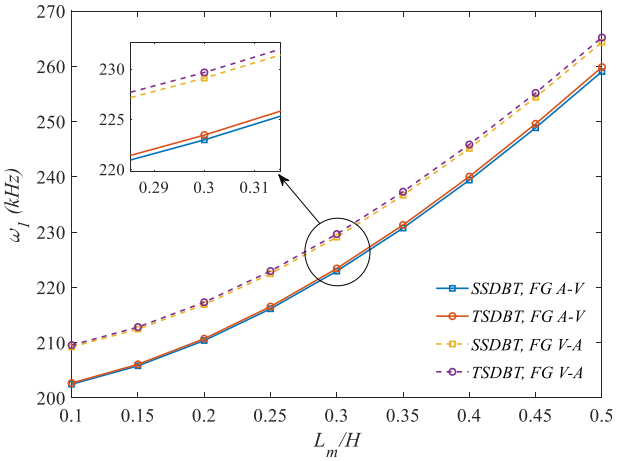

Fig. 7 Size effect on the fundamental natural frequency for SSDBT and Tan-SDBT

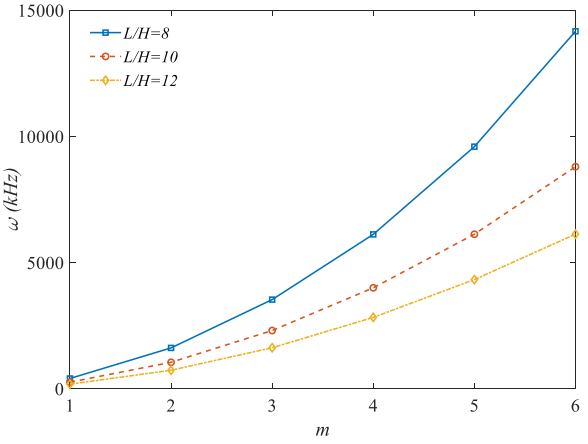

Fig. 8 Axial wave number effect for different aspect ratio values on the results

Table 5 Size effect for different volume fractions of CNTs on the natural frequencies (kHz)

V^*_{CNT}		L_m/H				
		0.1	0.2	0.3	0.4	0.5
0.12	SSDBT	205.8881	213.6697	226.0437	242.3059	261.7303
	Tan-SDBT	206.1498	214.0442	226.5628	242.9806	262.5640
0.17	SSDBT	230.6485	237.6717	248.9361	263.8976	281.9662
	Tan-SDBT	231.1783	238.3341	249.7548	264.8707	283.0873
0.28	SSDBT	273.4149	279.3989	289.0957	302.1464	318.1364
	Tan-SDBT	274.3596	280.5120	290.3924	303.6068	319.7389

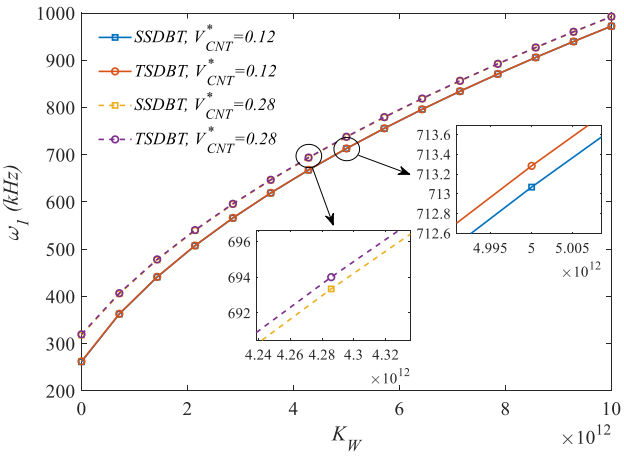

Fig. 9 Winkler coefficient of elastic foundation effect on the results

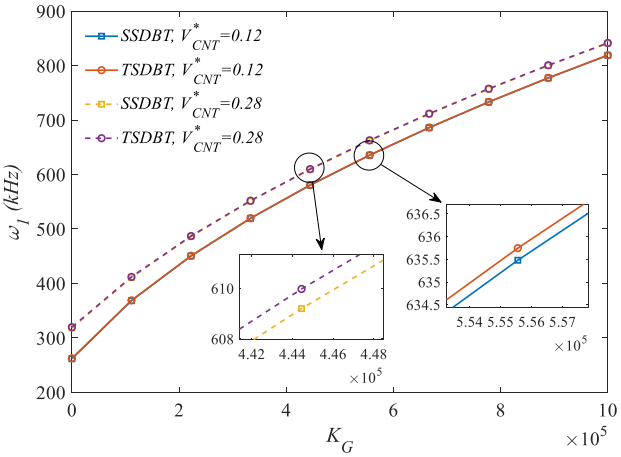

Fig. 10 Effect of shear layer coefficient on the natural frequency of the structure

2013, Dan *et al*. 2016, Ghorbanpour Arani *et al*. 2018). In this table, the thickness of the beam is considered as 0.2 *m*, its length is five times more than its thickness, the Poisson's ratio is 0.3, the elasticity modulus is 75 GPa, and the density of the structure is 2700 kg/m^3.

Regarding Table 1, it can be found that the results of the present study are in good convergence with those of literature. Noted that the little difference between the results of the present and previous studies is raised from different selected displacement fields and also different solution methods which lead to this difference. Therefore, the results of the current study are validated and in the following, the effect of the most important parameters on the vibrational behavior of a three-layered curved microbeam is presented.

5.2 Case study

To analyze the effect of the different parameters on the vibrational behavior of the under consideration microbeam, firstly the material properties of the FG porous core and FG CNTRCs face sheets are presented. The material type of the porous core is Tennessee marble with elasticity Young's modulus of 60 GPa and a density of 2700 kg/m^3. Also, its Poisson's ratio is 0.25. On the other hand, the matrix of the face sheets is from PVDF which has electro-mechanical properties and as stated before, the CNTs are chosen as the reinforcement. Material properties of the Polyvinylidene Fluoride (PVDF) and SWCNTs are presented in Table 2

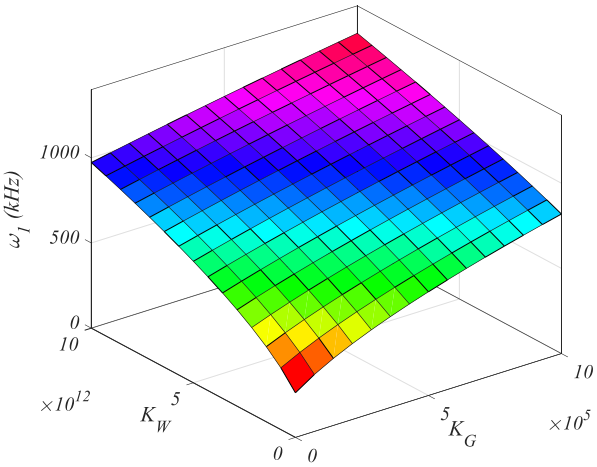

Fig. 11 Simultaneously consideration for effect of both Winkler and shear layer coefficients on the 1st natural frequency of the curved microbeam

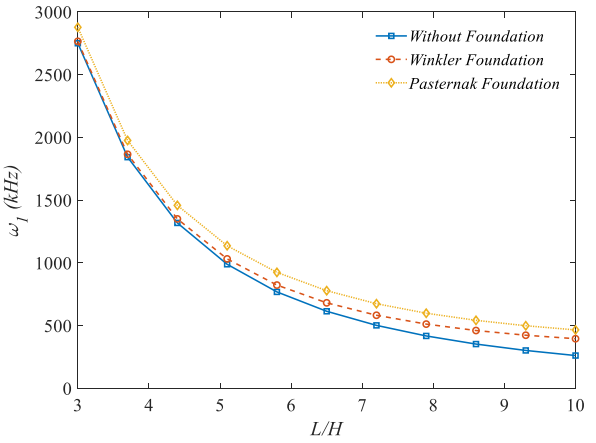

Fig. 12 Comparing different types of elastic foundation effect on the results

(Mohammadimehr *et al*. 2019).

Noted that as mentioned before, η_i (i = 1, 3) are efficiency parameters of CNTs that are different for each volume fraction. Therefore, for V_{CNT}^* = 0.12, η_1 = 0.137, and η_3 = 0.715, for V_{CNT}^* = 0.17, η_1 = 0.142 and η_3 = 1.138, and for V_{CNT}^* = 0.28, η_1 = 0.141 and η_3 = 1.109 (Amir *et al*. 2019). Also, it is noteworthy that generally the distribution of the pores is considered to be non-symmetric and the CNTs are distributed uniformly. Furthermore, the following specifications are used to extract the results: h_c = 100 μm, h_t = h_b = 10 μm, L = 10H, L_m = H/2, θ = π/6, e_1 = 0.3 and V_{CNT}^* = 0.12.

Table 3 illustrates the effect of porosity coefficient variations on the first three natural frequencies of the curved microbeam. It can be found that by increasing the porosity coefficient which indicates the pores to bulk volume ratio, the stiffness of the structure will be reduced more than its mass, and since the natural frequency is proportional to the square root of stiffness to mass ratio, so the natural frequency decreases too. Also, the results of Table 3 are presented based on both SSDBT and Tan-SDBT and can be seen that there is little difference between them.

Table 4 considers the effect of pores distribution type on the natural frequencies of the structure. The results are presented based on porosity coefficient variation and can be understood that the symmetric type of pores distribution leads to the most values of natural frequencies and the uniform type leads to the least ones. It may be raised due to their functions which are presented in Eqs. (20), (22) and (23).

Fig. 3 presents two effects: the first one is about CNTs distribution type and the second one is about the aspect ratio of the structure. by considering this figure, can be found that the FG V-A type has the maximum natural frequency and the FG A-V has the minimum ones among the considered distribution types. In fact, for FG V-A type, the CNTs are more in surfaces of the structure which enhances its stiffness but in FG A-V type, the CNTs are more about its mid-plane. So, the natural frequencies for this type are less than the others. On the other hand, by increasing the length of the curved microbeam rather than its thickness, the stiffness of the structure will be reduced, and accordingly, the frequencies will be decreased.

Fig. 4 depicts the effect of central angle θ and CNTs volume fraction values on the results. Based on the findings from this figure, increasing the central angle which means a reduction in curvature radius, leads the results to reduce, while increasing the volume fraction of CNTs leads them to enhance. CNTs' stiffness is much more than the matrix, consequently increasing their volume fraction than matrix, which will increase the face sheets stiffness, and in the following the stiffness of the structure will be increased which means an increase in the frequencies.

In Fig. 5, the effect of slenderness and the amount of CNTs is considered. Regarding this figure, can be seen that as the CNTs' amount increases with respect to the matrix phase, the natural frequencies increase, too. Also, as the beam becomes longer, it vibrates more.

The effect of thicknesses ratio is studied in Fig. 6. It is seen that by keeping the total thickness constant, increasing the core's thickness means a reduction to that of the face sheets. Since the face sheets, stiffness is much more than the core, so the reduction in their thickness will be ended to the reduction in stiffness of the whole of the structure. Therefore, the natural frequencies will be reduced. Also, the effect of pores distribution types can be seen in this figure which confirms the previous findings.

Size effect for two cases namely two CNTs distribution types and different values of CNTs volume fractions are considered in Fig. 7 and Table 5, respectively. Regarding these items, increasing the small-scale parameters L_m, the stiffness of the structure will be enhanced rapidly, and following it, the fundamental natural frequency of the structure will be increased.

Axial wave number increasing effect which shows the vibrational mode number is shown in Fig. 8 and as can be expected, its increasing leads the frequencies to enhance. This figure is plotted for different aspect ratios which ensure the previous findings.

The presented results up to here were in absence of an elastic foundation. But, now the effect of adding elastic

Table 6 Influence of different values of electro-mechanical preloads on the results (kHz)

V^*_{CNT}	P_0	ϕ_0									
		−200		−100		0		100		200	
		SSDBT	Tan-SDBT	SSDBT	Tan-SDBT	SSDBT	Tan-SDBT	SSDBT	Tan-SDBT	SSDBT	Tan-SDBT
0.12	−100	261.6676	262.5015	261.6412	262.4751	261.6147	262.4487	261.5882	262.4224	261.5618	262.3960
	0	261.7832	262.6167	261.7568	262.5903	261.7303	262.5640	261.7039	262.5376	261.6774	262.5112
	100	261.8987	262.7318	261.8723	262.7054	261.8459	262.6791	261.8194	262.6528	261.7930	262.6264
0.17	−100	281.9051	283.0264	281.8819	283.0033	281.8588	282.9803	281.8356	282.9571	281.8124	282.9340
	0	282.0126	283.1335	281.9894	283.1104	281.9662	283.0873	281.9430	283.0642	281.9198	283.0411
	100	282.1200	283.2404	282.0969	283.2173	282.0737	283.1943	282.0505	283.1712	282.0273	283.1481
0.28	−100	318.0766	319.6794	318.0587	319.6616	318.0408	319.6438	318.0229	319.6260	318.0050	319.6082
	0	318.1722	319.7745	318.1543	319.7567	318.1364	319.7389	318.1185	319.7211	318.1006	319.7033
	100	318.2677	319.8696	318.2498	319.8518	318.2319	319.8340	318.2141	319.8162	318.1962	319.7984

foundation and variation of its coefficients will be discussed. Fig. 9 shows the effect of the spring or Winkler coefficient increasing on the results. Increasing K_W enhances the stiffness of the structure and accordingly, the frequency will be reduced.

A similar effect but for K_G is considered in Fig. 10 and the variations of natural frequency are like that of K_W.

Fig. 11 shows the effect of both spring and shear layer coefficients simultaneously and can be found shear layer coefficient has more effect on the results than that of spring.

Also, Fig. 12 considered three different cases, namely without elastic foundation, with the Winkler elastic foundation which only consists of springs and Pasternak elastic foundation which consists of both springs and shear layer. It is understood that adding the elastic foundation enhances the stiffness and natural frequencies of the structure and adding the shear layer which converts the Winkler type to Pasternak one, has a similar effect on the vibrational behavior of the curved microbeam.

Finally, the effect of electro-mechanical preloads is considered and listed in Table 6. According to this table, the positive mechanical preload which means tensile load increases the stability of the structure, and following it, as the tensile load becomes more, the frequency will be enhanced. But for negative preload which means compressive load, makes the structure unstable and as the compressive load becomes more, the frequency will be reduced. It is noticeable that this effect is not significant. Moreover, about electrical preload, the positive applied potential leads the frequencies to be reduced, while the negative potential leads them to enhance due to increasing the stability of the structure.

6. Conclusions

In the current study, the free vibrational behavior of a three-layered curved microbeam is considered based on the two higher-order and trigonometric shear deformation theories namely SSDBT and Tan-SDBT. The core of the structure is made from FG porous materials and the face sheets are from FG CNTRCs which are exposed to the electric field. The three layers' mechanical properties are varied through their thickness following to given functions. Hamilton's principle is used to extract the motion equations and the MCST is used to capture the size effect. To solve the motion equations analytically, Navier's method is employed for a simply supported ends case and by validating the results for the simpler state with previous works, effects of different parameters on the behavior of the structure are considered and the following items can be concluded:

• Increasing the porosity coefficient leads the natural frequencies to reduce.

• Among the three different types of porosity distributions, symmetric and uniform types have the most and the least values of natural frequencies, respectively.

• FG V-A and FG A-V patterns of CNTs distribution have the maximum and minimum values of the results, respectively.

• Increasing the volume fraction of CNTs in the face sheets enhances the stiffness and accordingly the natural frequencies of the structure.

• Increasing the small scale parameter, lead the frequencies to enhance.

• Increasing the central angle of the curved microbeam causes a reduction in the natural frequencies.

• By keeping the thickness constant, as the length of the structure increases, the natural frequency will be reduced.

• Increasing the core's thickness and reducing the face sheets' ones, lead the frequency to reduce.

• Adding the elastic foundation to the structure increases its stiffness and frequencies.

• Frequencies of the Pasternak type of elastic foundation are higher than those of Winkler.

• Increasing the tensile mechanical preload, increases the natural frequencies, while it is vice versa about the compressive load.

• Although increasing the positive applied electrical preload reduces the natural frequencies, but the negative one enhances it.

The obtained results based on Tan-SDBT are generally more than those of SSDBT.

Acknowledgments

The authors would like to thank the reviewers for their valuable comments and suggestions to improve the clarity of this study.

Funding

The authors are thankful to the University of Kashan for supporting this work by Grant No. 988099/5.

References

Ait Atmane, H., Tounsi, A. and Bernard, F. (2017), "Effect of thickness stretching and porosity on mechanical response of a functionally graded beams resting on elastic foundations", *Int. J. Mech. Mater. Des.*, **13**(1), 71-84. https://doi.org/10.1007/s10999-015-9318-x.

Ajayan, P.M. and Zhou, O.Z. (2001), *Carbon Nanotubes*, Springer Berlin, Germany. https://doi.org/10.1007/3-540-39947-X_14.

Akbas, S.D. (2018), "Forced vibration analysis of cracked functionally graded microbeams", *Adv. Nano Res., Int. J.*, **6**(1), 39-55. https://doi.org/10.12989/anr.2018.6.1.039.

Alibeigloo, A. (2013), "Static analysis of functionally graded carbon nanotube-reinforced composite plate embedded in piezoelectric layers by using theory of elasticity", *Compos. Struct.*, **95**, 612-622. https://doi.org/10.1016/j.compstruct.2012.08.018.

Amir, S., Arshid, E. and Ghorbanpour Arani, M.R. (2019), "Size-dependent magneto-electro-elastic vibration analysis of FG saturated porous annular/circular micro sandwich plates embedded with nano-composite face sheets subjected to multi-physical pre loads", *Smart Struct. Syst., Int. J.*, **23**(5), 429-447. https://doi.org/10.12989/sss.2019.23.5.429.

Anumandla, V. and Gibson, R.F. (2006), "A comprehensive closed form micromechanics model for estimating the elastic modulus of nanotube-reinforced composites", *Compos. Part A Appl. Sci. Manuf.*, **37**(12), 2178-2185. https://doi.org/10.1016/J.COMPOSITESA.2005.09.016.

Arshid, E. and Khorshidvand, A.R. (2018), "Free vibration analysis of saturated porous FG circular plates integrated with piezoelectric actuators via differential quadrature method", *Thin-Wall. Struct.*, **125**, 220-233. https://doi.org/10.1016/j.tws.2018.01.007.

Arshid, E., Khorshidvand, A.R. and Khorsandijou, S.M. (2019a), "The effect of porosity on free vibration of SPFG circular plates resting on visco-Pasternak elastic foundation based on CPT, FSDT and TSDT", *Struct. Eng. Mech., Int. J.*, **70**(1), 97-112. https://dx.doi.org/10.12989/sem.2019.70.1.097.

Arshid, E., Kiani, A. and Amir, S. (2019b), "Magneto-electro-elastic vibration of moderately thick FG annular plates subjected to multi physical loads in thermal environment using GDQ method by considering neutral surface", *Proc. Inst. Mech. Eng. Part L J. Mater. Des. Appl.*, **233**(10), 2140-1259. https://doi.org/10.1177/1464420719832626.

Arshid, E., Amir, S. and Loghman, A. (2020a), "Static and dynamic analyses of FG-GNPs reinforced porous nanocomposite annular micro-plates based on MSGT", *Int. J. Mech. Sci.*, **180**, 105656. https://doi.org/10.1016/j.ijmecsci.2020.105656.

Arshid, E., Amir, S. and Loghman, A. (2020b), "Bending and buckling behaviors of heterogeneous temperature-dependent micro annular/circular porous sandwich plates integrated by FGPEM nano-Composite layers", *J. Sandw. Struct. Mater.*, **2016**, 109963622095502. https://doi.org/10.1177/1099636220955027.

Barati, M.R. and Zenkour, A.M. (2017), "Investigating post-buckling of geometrically imperfect metal foam nanobeams with symmetric and asymmetric porosity distributions", *Compos. Struct.*, **182**, 91-98. https://doi.org/10.1016/J.COMPSTRUCT.2017.09.008.

Bendaho, B., Belabed, Z., Bourada, M., Benatta, M.A., Bourada, F. and Tounsi, A. (2019), "Assessment of new 2D and quasi-3D Nonlocal theories for free vibration analysis of size-dependent functionally graded (FG) nanoplates", *Adv. Nano Res., Int. J.*, **7**(4), 277-292. https://doi.org/10.12989/anr.2019.7.4.277.

Benmansour, D.L., Kaci, A., Bousahla, A.A., Heireche, H., Tounsi, A., Alwabli, A.S. and Mahmoud, S.R. (2019), "The nano scale bending and dynamic properties of isolated protein microtubules based on modified strain gradient theory", *Adv. Nano Res., Int. J.*, **7**(6), 443-457. https://doi.org/10.12989/anr.2019.7.6.443.

Berghouti, H., Adda Bedia, E.A., Benkhedda, A. and Tounsi, A. (2019), "Vibration analysis of nonlocal porous nanobeams made of functionally graded material", *Adv. Nano Res., Int. J.*, **7**(5), 351-364. https://doi.org/10.12989/anr.2019.7.5.351.

Bui, T.Q., Nguyen, M.N. and Zhang, C. (2011), "An efficient meshfree method for vibration analysis of laminated composite plates", *Computat. Mech.*, **48**(2), 175-193. https://doi.org/10.1007/s00466-011-0591-8.

Bui, T.Q., Khosravifard, A., Zhang, C., Hematiyan, M.R. and Golub, M.V. (2013), "Dynamic analysis of sandwich beams with functionally graded core using a truly meshfree radial point interpolation method", *Eng. Struct.*, **47**, 90-104. https://doi.org/10.1016/j.engstruct.2012.03.041.

Chen, D., Yang, J. and Kitipornchai, S. (2015), "Elastic buckling and static bending of shear deformable functionally graded porous beam", *Compos. Struct.*, **133**, 54-61. https://doi.org/10.1016/J.COMPSTRUCT.2015.07.052.

Dan, M., Pagani, A. and Carrera, E. (2016), "Free vibration analysis of simply supported beams with solid and thin-walled cross-sections using higher-order theories based on displacement variables", *Thin-Wall. Struct.*, **98**, 478-495. https://doi.org/10.1016/J.TWS.2015.10.012.

Detournay, E. and Cheng, A.H.D. (1993), "Fundamentals of Poroelasticity", *Analysis Des. Methods*, 113-171. https://doi.org/10.1016/B978-0-08-040615-2.50011-3.

Duc, N.D., Cong, P.H., Tuan, N.D., Tran, P. and Thanh, N.V. (2017), "Thermal and mechanical stability of functionally graded carbon nanotubes (FG-CNT)-reinforced composite truncated conical shells surrounded by the elastic foundations", *Thin-Wall. Struct.*, **115**, 300-310. https://doi.org/10.1016/J.TWS.2017.02.016.

Ebrahimi, F. and Mokhtari, M. (2015), "Transverse vibration analysis of rotating porous beam with functionally graded microstructure using the differential transform method", *J. Braz. Soc. Mech. Sci. Eng.*, **37**(4), 1435-1444. https://doi.org/10.1007/s40430-014-0255-7.

Ebrahimi, F. and Jafari, A. (2016), "Thermo-mechanical vibration analysis of temperature-dependent porous FG beams based on Timoshenko beam theory", *Struct. Eng. Mech., Int. J.*, **59**(2), 343-371. https://dx.doi.org/10.12989/sem.2016.59.2.343.

Ebrahimi, F. and Barati, M.R. (2017), "Size-dependent vibration analysis of viscoelastic nanocrystalline silicon nanobeams with porosities based on a higher order refined beam theory", *Compos. Struct.*, **166**, 256-267. https://doi.org/10.1016/J.COMPSTRUCT.2017.01.036.

Ebrahimi, F., Jafari, A. and Barati, M.R. (2017), "Vibration analysis of magneto-electro-elastic heterogeneous porous material plates resting on elastic foundations", *Thin-Wall.*

Struct., **119**, 33-46. https://doi.org/10.1016/J.TWS.2017.04.002.
Eringen, A.C. (1983), "On differential equations of nonlocal elasticity and solutions of screw dislocation and surface waves", *J. Appl. Phys*., **54**(9), 4703-4710. https://doi.org/10.1063/1.332803.
Eringen, A.C. (2002). *Nonlocal Continuum Field Theories*, Springer Science & Business Media, USA.
Fang, W., Yu, T., Van Lich, L. and Bui, T.Q. (2019), "Analysis of thick porous beams by a quasi-3D theory and isogeometric analysis", *Compos. Struct*., **221**, 110890. https://doi.org/10.1016/j.compstruct.2019.04.062.
Ghorbanpour Arani, A. and Haghparast, E. (2017), "Size-dependent vibration of axially moving viscoelastic micro-plates based on sinusoidal shear deformation theory", *Int. J. Appl. Mech*., **9**(2), 1750026. https://doi.org/10.1142/S1758825117500260.
Ghorbanpour Arani, A., BabaAkbar-Zarei, H., Pourmousa, P. and Eskandari, M. (2018), "Investigation of free vibration response of smart sandwich micro-beam on Winkler-Pasternak substrate exposed to multi physical fields", *Microsyst. Technol*., **24**(7), 3045-3060. https://doi.org/10.1007/s00542-017-3681-5.
Hadji, L., Atmane, H.A., Tounsi, A., Mechab, I. and Addabedia, E.A. (2011), "Free vibration of functionally graded sandwich plates using four-variable refined plate theory", *Appl. Math. Mech*., **32**(7), 925-942. https://doi.org/10.1007/s10483-011-1470-9.
Han, Y. and Elliott, J. (2007), "Molecular dynamics simulations of the elastic properties of polymer/carbon nanotube composites", *Comput. Mater. Sci*., **39**(2), 315-323. https://doi.org/10.1016/J.COMMATSCI.2006.06.011.
Iijima, S. (1991), "Helical microtubules of graphitic carbon", *Nature*, **354**(6348), 56. https://doi.org/10.1038/354056a0.
Jafari, A. and Ezzati, M. (2017), "Investigating the non-classical boundary conditions relevant to strain gradient theories", *Physica E Low Dimens. Syst. Nanostruct*., **86**, 88-102. https://doi.org/10.1016/J.PHYSE.2016.09.012.
Jafari, A., Shirvani Shah-enayati, S. and Atai, A.A. (2016), "Size dependency in vibration analysis of nano plates; one problem, different answers", *Eur. J. Mech. A/Solids*, **59**, 124-139. https://doi.org/10.1016/J.EUROMECHSOL.2016.03.011.
Kitipornchai, S., Chen, D. and Yang, J. (2017), "Free vibration and elastic buckling of functionally graded porous beams reinforced by graphene platelets", *Mater. Des*., **116**, 656-665. https://doi.org/10.1016/J.MATDES.2016.12.061.
Lei, Z.X., Liew, K.M. and Yu, J.L. (2013), "Buckling analysis of functionally graded carbon nanotube-reinforced composite plates using the element-free kp-Ritz method", *Compos. Struct*., **98**, 160-168. https://doi.org/10.1016/J.COMPSTRUCT.2012.11.006.
Liu, Y.P. and Reddy, J.N. (2011), "A nonlocal curved beam model based on a modified couple stress theory", *Int. J. Struct. Stab. Dyn*., **11**(3), 495-512. https://doi.org/10.1142/s0219455411004233.
Liu, P. and Chen, G.F. (2014), *Porous Materials: Processing and Applications*. Elsevier, New York, USA.
Liu, S., Yu, T. and Bui, T.Q. (2017), "Size effects of functionally graded moderately thick microplates: A novel non-classical simple-FSDT isogeometric analysis", *Eur. J. Mech. A/Solids*, **66**, 446-458. https://doi.org/10.1016/j.euromechsol.2017.08.008.
Liu, S., Yu, T., Van Lich, L., Yin, S. and Bui, T.Q. (2018), "Size effect on cracked functional composite micro-plates by an XIGA-based effective approach", *Meccanica*, **53**(10), 2637-2658. https://doi.org/10.1007/s11012-018-0848-9.
Liu, S., Yu, T., Lich, L.V., Yin, S. and Bui, T.Q. (2019), "Size and surface effects on mechanical behavior of thin nanoplates incorporating microstructures using isogeometric analysis", *Comput. Struct*., **212**, 173-187. https://doi.org/10.1016/j.compstruc.2018.10.009.
Lunhui, G., Kazu, S. and Iijima, S. (2008), "Smallest carbon nanotube assigned with atomic resolution accuracy", *Nano Lett*., **8**(2), 459-462. https://doi.org/10.1021/NL072396J.
Magnucki, K. and Stasiewicz, P. (2004), "Elastic buckling of a porous beam", *J. Theor. Appl. Mech*., **42**(4), 859-868.
Malekzadeh, P. and Shojaee, M. (2013), "Buckling analysis of quadrilateral laminated plates with carbon nanotubes reinforced composite layers", *Thin-Wall. Struct*., **71**, 108-118. https://doi.org/10.1016/J.TWS.2013.05.008.
McEvoy, M.A. and Correll, N. (2015), "Materials that couple sensing, actuation, computation, and communication", *Science*, **347**(6228), 1261689. https://doi.org/10.1126/science.1261689.
Mehar, K. and Panda, S.K. (2019), "Multiscale modeling approach for thermal buckling analysis of nanocomposite curved structure", *Adv. Nano Res., Int. J*., **7**(3), 181-190. https://doi.org/10.12989/anr.2019.7.3.181.
Mirjavadi, S.S., Forsat, M., Nia, A.F., Badnava, S. and Hamouda, A.M.S. (2020), "Nonlocal strain gradient effects on forced vibrations of porous FG cylindrical nanoshells", *Adv. Nano Res*., **8**(2), 149-156. https://doi.org/10.12989/anr.2020.8.2.149.
Mohammadimehr, M., Arshid, E., Alhosseini, S.M.A.R., Amir, S. and Arani, M.R.G. (2019), "Free vibration analysis of thick cylindrical MEE composite shells reinforced CNTs with temperature-dependent properties resting on viscoelastic foundation", *Struct. Eng. Mech., Int. J*., **70**(6), 683-702. https://doi.org/10.12989/sem.2019.70.6.683.
Pagani, A., Boscolo, M., Banerjee, J.R. and Carrera, E. (2013), "Exact dynamic stiffness elements based on one-dimensional higher-order theories for free vibration analysis of solid and thin-walled structures", *J. Sound Vib*., **332**(23), 6104-6127. https://doi.org/10.1016/j.jsv.2013.06.023.
Panah, M., Khorshidvand, A.R., Khorsandijou, S.M. and Jabbari, M. (2019), "Pore pressure and porosity effects on bending and thermal postbuckling behavior of FG saturated porous circular plates", *J. Therm. Stresses*, **2019**, 1-27. https://doi.org/10.1080/01495739.2019.1614502.
Shafiei, N. and Kazemi, M. (2017), "Nonlinear buckling of functionally graded nano-/micro-scaled porous beams", *Compos. Struct*., **178**, 483-492. https://doi.org/10.1016/J.COMPSTRUCT.2017.07.045.
Shahsavari, D., Karami, B. and Janghorban, M. (2019), "Size-dependent vibration analysis of laminated composite plates", *Adv. Nano Res., Int. J*., **7**(5), 337-349. https://doi.org/10.12989/anr.2019.7.5.337.
Shen, H.S. (2011), "Postbuckling of nanotube-reinforced composite cylindrical shells in thermal environments, part I: Axially-loaded shells", *Compos. Struct*., **93**(8), 2096-2108. https://doi.org/10.1016/j.compstruct.2011.02.011.
Shen, H.S. (2012), "Thermal buckling and postbuckling behavior of functionally graded carbon nanotube-reinforced composite cylindrical shells", *Compos. Part B: Eng*., **43**(3), 1030-1038. https://doi.org/10.1016/J.COMPOSITESB.2011.10.004.
Sobhy, M. and Zenkour, A.M. (2018), "Magnetic field effect on thermomechanical buckling and vibration of viscoelastic sandwich nanobeams with CNT reinforced face sheets on a viscoelastic substrate", *Compos. Part B Eng*., **154**, 492-506. https://doi.org/10.1016/J.COMPOSITESB.2018.09.011.
Tayeb, T.S., Zidour, M., Bensattalah, T., Heireche, H., Benahmed, A. and Bedia, E.A. (2020), "Mechanical buckling of FG-CNTs reinforced composite plate with parabolic distribution using Hamilton's energy principle", *Adv. Nano Res., Int. J*., **8**(2), 135-148. https://doi.org/10.12989/anr.2020.8.2.135.
Thostenson, E.T. and Chou, T.W. (2003), "On the elastic properties of carbon nanotube-based composites: Modelling and characterization", *J. Phys. D Appl. Phys*., **36**(5), 573. https://doi.org/10.1088/0022-3727/36/5/323.

Von Terzaghi, K. (1923), "Die Berechnug der Durchlassigkeit des Tones aus dem Verlauf der hydromechanischen Spannungserscheinungen", *Sitzungsber. Akad. Wiss. Math. Naturwiss. Kl., Abt. Iia*, **132**, 125-138.

Wattanasakulpong, N. and Ungbhakorn, V. (2012), "Free vibration analysis of functionally graded beams with general elastically end constraints by DTM", *World J. Mech.*, **2**(6), 297-310. https://doi.org/10.4236/wjm.2012.26036.

Yu, T., Hu, H., Zhang, J. and Bui, T.Q. (2019a), "Isogeometric analysis of size-dependent effects for functionally graded microbeams by a non-classical quasi-3D theory", *Thin-Wall. Struct.*, **138**, 1-14. https://doi.org/10.1016/j.tws.2018.12.006.

Yu, T., Zhang, J., Hu, H. and Bui, T.Q. (2019b), "A novel size-dependent quasi-3D isogeometric beam model for two-directional FG microbeams analysis", *Compos. Struct.*, **211**, 76-88. https://doi.org/10.1016/j.compstruct.2018.12.014.

Zhu, P., Lei, Z.X. and Liew, K.M. (2012), "Static and free vibration analyses of carbon nanotube-reinforced composite plates using finite element method with first order shear deformation plate theory", *Compos. Struct.*, **94**(4), 1450-1460. https://doi.org/10.1016/j.compstruct.2011.11.010.

AT

Appendix

The non-zero components of stiffness and mass matrices introduced in Eq. (47) are defined as follow.

$$K_{11}=\frac{Q_{550}}{R^2}+\frac{G_0}{R^2}+Q_{110}\alpha^2+A_{10}\alpha^2+\frac{{L_m}^2H_1\alpha^2}{4R^2}+\frac{{L_m}^2T_1\alpha^2}{4R^2}$$

$$K_{12}=-Q_{111}\alpha^3-A_{11}\alpha^3-\frac{{L_m}^2H_1\alpha^3}{2R}-\frac{{L_m}^2H_2\alpha^3}{4R^2}-\frac{{L_m}^2T_1\alpha^3}{2R}-\frac{{L_m}^2T_2\alpha^3}{4R^2}-\frac{A_{10}\alpha}{R}-\frac{Q_{110}\alpha}{R}-\frac{Q_{551}\alpha}{R^2}-\frac{G_1\alpha}{R^2}$$

$$K_{13}=\frac{Q_{556}}{R}+\frac{Q_{553}}{R^2}+\frac{G_6}{R}+\frac{G_3}{R^2}+Q_{113}\alpha^2+A_{13}\alpha^2+\frac{{L_m}^2H_7\alpha^2}{4R}+\frac{{L_m}^2H_4\alpha^2}{4R^2}+\frac{{L_m}^2T_7\alpha^2}{4R}+\frac{{L_m}^2T_4\alpha^2}{4R^2}$$

$$K_{21}=-Q_{111}\alpha^3-A_{11}\alpha^3-\frac{{L_m}^2T_2\alpha^3}{4R^2}-\frac{{L_m}^2H_1\alpha^3}{2R}-\frac{{L_m}^2T_1\alpha^3}{2R}-\frac{{L_m}^2H_2\alpha^3}{4R^2}-\frac{Q_{110}\alpha}{R}-\frac{A_{10}\alpha}{R}-\frac{Q_{551}\alpha}{R^2}-\frac{G_1\alpha}{R^2}$$

$$K_{23}=-\frac{G_5\alpha}{R^2}-\frac{1}{2}{L_m}^2H_7\alpha^3-\frac{1}{2}{L_m}^2T_7\alpha^3-Q_{115}\alpha^3-A_{15}\alpha^3-\frac{{L_m}^2T_8\alpha^3}{4R}-\frac{{L_m}^2T_6\alpha^3}{4R^2}-\frac{{L_m}^2H_{11}\alpha}{4R}-\frac{{L_m}^2H_7\alpha}{4R^2}$$
$$-\frac{{L_m}^2T_{11}\alpha}{4R}-\frac{{L_m}^2T_7\alpha}{4R^2}-\frac{{L_m}^2T_4\alpha^3}{2R}-\frac{{L_m}^2H_4\alpha^3}{2R}-\frac{{L_m}^2H_8\alpha^3}{4R}-\frac{{L_m}^2H_6\alpha^3}{4R^2}-\frac{Q_{113}\alpha}{R}-\frac{A_{13}\alpha}{R}-\frac{Q_{557}\alpha}{R}-\frac{Q_{555}\alpha}{R^2}-\frac{G_7\alpha}{R}$$

$$K_{22}=2\frac{Q_{111}\alpha^2}{R}+2\frac{A_{11}\alpha^2}{R}+{L_m}^2H_1\alpha^4+{L_m}^2T_1\alpha^4-K_W+\frac{Q_{110}}{R^2}+\frac{A_{10}}{R^2}+Q_{112}\alpha^4+A_{12}\alpha^4-K_G\alpha^2-N^{ext}\alpha^2+\frac{{L_m}^2T_3\alpha^4}{4R^2}$$
$$+\frac{{L_m}^2H_1\alpha^2}{4R^2}+\frac{{L_m}^2T_1\alpha^2}{4R^2}+\frac{{L_m}^2T_2\alpha^4}{R}+\frac{{L_m}^2H_2\alpha^4}{R}+\frac{{L_m}^2H_3\alpha^4}{4R^2}+\frac{Q_{552}\alpha^2}{R^2}+\frac{G_2\alpha^2}{R^2}$$

$$K_{33}=G_9+Q_{559}+\frac{T_9{L_m}^2\alpha^2}{4R}+\frac{H_9{L_m}^2\alpha^2}{4R}+\frac{{L_m}^2H_{13}}{2R}+\frac{{L_m}^2T_{13}}{2R}+\frac{{L_m}^2H_{10}}{4R^2}+\frac{{L_m}^2T_{10}}{4R^2}+\frac{1}{4}{L_m}^2H_{10}\alpha^2+\frac{1}{4}{L_m}^2T_{10}\alpha^2+\frac{G_4}{R^2}$$
$$+\frac{1}{4}{L_m}^2T_{12}+2\frac{G_8}{R}+2\frac{Q_{558}}{R}+\frac{1}{4}{L_m}^2H_{12}+\frac{Q_{554}}{R^2}+\frac{{L_m}^2H_9\alpha^2}{4R}+\frac{{L_m}^2H_5\alpha^2}{4R^2}+\frac{{L_m}^2T_9\alpha^2}{4R}+\frac{{L_m}^2T_5\alpha^2}{4R^2}$$

$$K_{32}=-\frac{T_8{L_m}^2\alpha^3}{4R}-\frac{T_{11}{L_m}^2\alpha}{4R}-\frac{H_8{L_m}^2\alpha^3}{4R}-\frac{H_{11}{L_m}^2\alpha}{4R}-\frac{G_7\alpha}{R}-\frac{Q_{557}\alpha}{R}-\frac{1}{2}{L_m}^2H_7\alpha^3-\frac{Q_{555}\alpha}{R^2}-\frac{G_5\alpha}{R^2}-\frac{1}{2}{L_m}^2T_7\alpha^3$$
$$-\frac{{L_m}^2H_4\alpha^3}{2R}-\frac{{L_m}^2H_6\alpha^3}{4R^2}-\frac{{L_m}^2T_4\alpha^3}{2R}-\frac{{L_m}^2T_6\alpha^3}{4R^2}-\frac{H_7{L_m}^2\alpha}{4R^2}-\frac{T_7{L_m}^2\alpha}{4R^2}$$

$$K_{14}=-E_{310}\alpha-\frac{E_{150}\alpha}{R},\qquad K_{24}=\frac{E_{310}}{R}+E_{311}\alpha^2+\frac{E_{151}\alpha^2}{R}$$

$$K_{31}=\frac{G_3}{R^2}+\frac{G_6}{R}+\frac{Q_{556}}{R}+\frac{Q_{553}}{R^2}+\frac{{L_m}^2H_4\alpha^2}{4R^2}+\frac{{L_m}^2T_4\alpha^2}{4R^2}+\frac{H_7{L_m}^2\alpha^2}{4R}+\frac{T_7{L_m}^2\alpha^2}{4R}$$

$$K_{41}=-E_{310}\alpha-\frac{E_{150}\alpha}{R},\qquad K_{34}=-\frac{E_{153}\alpha}{R}-E_{156}\alpha$$

$$K_{43}=-E_{159}\alpha-\frac{E_{153}\alpha}{R}-E_{313}\alpha$$

$$K_{42}=\frac{E_{310}}{R}+E_{311}\alpha^2+\frac{E_{151}\alpha^2}{R},\qquad K_{44}=-S_{110}\alpha^2-S_{330},\qquad M_{11}=-I_0,\qquad M_{12}=M_{21}=I_1\alpha$$

$$M_{13}=M_{31}=-I_3,\qquad M_{22}=-I_2\alpha^2-I_0,\qquad M_{23}=M_{32}=I_5\alpha,\qquad M_{33}=-I_4$$

in which

$$Q_{11i}=\int_{-\frac{h_c}{2}-h_b}^{-\frac{h_c}{2}}Q_{11}z^i dz+\int_{\frac{h_c}{2}}^{\frac{h_c}{2+h_t}}Q_{11}z^i dz,\qquad i=0,1,2$$

$$Q_{113}=\int_{-\frac{h_c}{2}-h_b}^{-\frac{h_c}{2}}Q_{11}f(z)dz+\int_{\frac{h_c}{2}}^{\frac{h_c}{2+h_t}}Q_{11}f(z)dz$$

$$Q_{114}=\int_{-\frac{h_c}{2}-h_b}^{-\frac{h_c}{2}}Q_{11}f^2(z)dz+\int_{\frac{h_c}{2}}^{\frac{h_c}{2+h_t}}Q_{11}f^2(z)dz$$

$$Q_{115}=\int_{-\frac{h_c}{2}-h_b}^{-\frac{h_c}{2}}Q_{11}zf(z)dz+\int_{\frac{h_c}{2}}^{\frac{h_c}{2+h_t}}Q_{11}zf(z)dz$$

$$Q_{55i}=\int_{-\frac{h_c}{2}-h_b}^{-\frac{h_c}{2}}Q_{55}z^i dz+\int_{\frac{h_c}{2}}^{\frac{h_c}{2+h_t}}Q_{55}z^i dz,\qquad i=0,1,2$$

$$Q_{553}=\int_{-\frac{h_c}{2}-h_b}^{-\frac{h_c}{2}}Q_{55}f(z)dz+\int_{\frac{h_c}{2}}^{\frac{h_c}{2+h_t}}Q_{55}f(z)dz$$

$$Q_{554}=\int_{-\frac{h_c}{2}-h_b}^{-\frac{h_c}{2}}Q_{55}f^2(z)dz+\int_{\frac{h_c}{2}}^{\frac{h_c}{2+h_t}}Q_{55}f^2(z)dz$$

$$Q_{555}=\int_{-\frac{h_c}{2}-h_b}^{-\frac{h_c}{2}}Q_{55}zf(z)dz+\int_{\frac{h_c}{2}}^{\frac{h_c}{2+h_t}}Q_{55}zf(z)dz$$

$$Q_{556}=\int_{-\frac{h_c}{2}-h_b}^{-\frac{h_c}{2}}Q_{55}\frac{df(z)}{dz}dz+\int_{\frac{h_c}{2}}^{\frac{h_c}{2+h_t}}Q_{55}\frac{df(z)}{dz}dz$$

$$Q_{557}=\int_{-\frac{h_c}{2}-h_b}^{-\frac{h_c}{2}}Q_{55}z\frac{df(z)}{dz}dz+\int_{\frac{h_c}{2}}^{\frac{h_c}{2+h_t}}Q_{55}z\frac{df(z)}{dz}dz$$

$$Q_{558}=\int_{-\frac{h_c}{2}-h_b}^{-\frac{h_c}{2}}Q_{55}f(z)\frac{df(z)}{dz}dz+\int_{\frac{h_c}{2}}^{\frac{h_c}{2+h_t}}Q_{55}f(z)\frac{df(z)}{dz}dz$$

$$Q_{559}=\int_{-\frac{h_c}{2}-h_b}^{-\frac{h_c}{2}}Q_{55}\left(\frac{df(z)}{dz}\right)^2dz+\int_{\frac{h_c}{2}}^{\frac{h_c}{2+h_t}}Q_{55}\left(\frac{df(z)}{dz}\right)^2dz$$

$$A_{1i}=\int_{-\frac{h_c}{2}}^{\frac{h_c}{2}}A(z)z^i dz\,,\qquad i=0,1,2,\qquad A_{13}=\int_{-\frac{h_c}{2}}^{\frac{h_c}{2}}A(z)f(z)dz\,,\qquad A_{14}=\int_{-\frac{h_c}{2}}^{\frac{h_c}{2}}A(z)f^2(z)dz$$

$$A_{15}=\int_{-\frac{h_c}{2}}^{\frac{h_c}{2}}A(z)zf(z)dz\,,\qquad G_0=\int_{-\frac{h_c}{2}}^{\frac{h_c}{2}}G(z)z^i dz\,,\qquad i=0,1,2,\qquad G_3=\int_{-\frac{h_c}{2}}^{\frac{h_c}{2}}G(z)f(z)dz$$

$$G_4=\int_{-\frac{h_c}{2}}^{\frac{h_c}{2}}G(z)f^2(z)dz\,,\qquad G_5=\int_{-\frac{h_c}{2}}^{\frac{h_c}{2}}G(z)zf(z)dz\,,\qquad G_6=\int_{-\frac{h_c}{2}}^{\frac{h_c}{2}}G(z)\frac{df(z)}{dz}dz$$

$$G_7=\int_{-\frac{h_c}{2}}^{\frac{h_c}{2}}G(z)z\frac{df(z)}{dz}dz\,,\qquad G_8=\int_{-\frac{h_c}{2}}^{\frac{h_c}{2}}G(z)f(z)\frac{df(z)}{dz}dz\,,\qquad G_9=\int_{-\frac{h_c}{2}}^{\frac{h_c}{2}}G(z)\left(\frac{df(z)}{dz}\right)^2dz$$

$$E_{310}=\int_{-\frac{h_c}{2}-h_b}^{-\frac{h_c}{2}}\frac{\pi}{h_b}e_{31}\sin\left(\frac{\pi z_b}{h_b}\right)dz+\int_{\frac{h_c}{2}}^{\frac{h_c}{2+h_t}}\frac{\pi}{h_t}e_{31}\sin\left(\frac{\pi z_t}{h_t}\right)dz$$

$$E_{311}=\int_{-\frac{h_c}{2}-h_b}^{-\frac{h_c}{2}}\frac{\pi}{h_b}e_{31}\sin\left(\frac{\pi z_b}{h_b}\right)zdz+\int_{\frac{h_c}{2}}^{\frac{h_c}{2+h_t}}\frac{\pi}{h_t}e_{31}\sin\left(\frac{\pi z_t}{h_t}\right)zdz$$

$$E_{313}=\int_{-\frac{h_c}{2}-h_b}^{-\frac{h_c}{2}}\frac{\pi}{h_b}e_{31}\sin\left(\frac{\pi z_b}{h_b}\right)f(z)dz+\int_{\frac{h_c}{2}}^{\frac{h_c}{2+h_t}}\frac{\pi}{h_t}e_{31}\sin\left(\frac{\pi z_t}{h_t}\right)f(z)dz$$

$$E_{150}=\int_{-\frac{h_c}{2}-h_b}^{-\frac{h_c}{2}}e_{15}\cos\left(\frac{\pi z_b}{h_b}\right)dz+\int_{\frac{h_c}{2}}^{\frac{h_c}{2+h_t}}e_{15}\cos\left(\frac{\pi z_t}{h_t}\right)dz$$

$$E_{151}=\int_{-\frac{h_c}{2}-h_b}^{-\frac{h_c}{2}}e_{15}\cos\left(\frac{\pi z_b}{h_b}\right)zdz+\int_{\frac{h_c}{2}}^{\frac{h_c}{2+h_t}}e_{15}\cos\left(\frac{\pi z_t}{h_t}\right)zdz$$

$$E_{153}=\int_{-\frac{h_c}{2}-h_b}^{-\frac{h_c}{2}}e_{15}\cos\left(\frac{\pi z_b}{h_b}\right)f(z)dz+\int_{\frac{h_c}{2}}^{\frac{h_c}{2+h_t}}e_{15}\cos\left(\frac{\pi z_t}{h_t}\right)f(z)dz$$

$$E_{156}=\int_{-\frac{h_c}{2}-h_b}^{-\frac{h_c}{2}}e_{15}\cos\left(\frac{\pi z_b}{h_b}\right)\left(\frac{df(z)}{dz}\right)dz+\int_{\frac{h_c}{2}}^{\frac{h_c}{2+h_t}}e_{15}\cos\left(\frac{\pi z_t}{h_t}\right)\left(\frac{df(z)}{dz}\right)dz$$

$$E_{159}=\int_{-\frac{h_c}{2}-h_b}^{-\frac{h_c}{2}}e_{15}\cos\left(\frac{\pi z_b}{h_b}\right)\left(\frac{df(z)}{dz}\right)^2dz+\int_{\frac{h_c}{2}}^{\frac{h_c}{2+h_t}}e_{15}\cos\left(\frac{\pi z_t}{h_t}\right)\left(\frac{df(z)}{dz}\right)^2dz$$

$$S_{110}=\int_{-\frac{h_c}{2}-h_b}^{-\frac{h_c}{2}}S_{11}\cos^2\left(\frac{\pi z_b}{h_b}\right)dz+\int_{\frac{h_c}{2}}^{\frac{h_c}{2+h_t}}S_{11}\cos^2\left(\frac{\pi z_t}{h_t}\right)dz$$

$$S_{330}=\int_{-\frac{h_c}{2}-h_b}^{-\frac{h_c}{2}}S_{33}\left(\frac{\pi}{h_b}\right)^2\sin^2\left(\frac{\pi z_b}{h_b}\right)dz+\int_{\frac{h_c}{2}}^{\frac{h_c}{2+h_t}}S_{33}\left(\frac{\pi}{h_t}\right)^2\sin^2\left(\frac{\pi z_t}{h_t}\right)dz$$

$$H_1 = \int_{-\frac{h_c}{2}-h_b}^{-\frac{h_c}{2}} \mu_b(z) z^i dz + \int_{\frac{h_c}{2}}^{\frac{h_c}{2+h_t}} \mu_t(z) z^i dz, \qquad i = 0,1,2$$

$$H_4 = \int_{-\frac{h_c}{2}-h_b}^{-\frac{h_c}{2}} \mu_b(z) f(z) dz + \int_{\frac{h_c}{2}}^{\frac{h_c}{2+h_t}} \mu_t(z) f(z) dz$$

$$H_5 = \int_{-\frac{h_c}{2}-h_b}^{-\frac{h_c}{2}} \mu_b(z) f^2(z) dz + \int_{\frac{h_c}{2}}^{\frac{h_c}{2+h_t}} \mu_t(z) f^2(z) dz$$

$$H_6 = \int_{-\frac{h_c}{2}-h_b}^{-\frac{h_c}{2}} \mu_b(z) z f(z) dz + \int_{\frac{h_c}{2}}^{\frac{h_c}{2+h_t}} \mu_t(z) z f(z) dz$$

$$H_7 = \int_{-\frac{h_c}{2}-h_b}^{-\frac{h_c}{2}} \mu_b(z) \left(\frac{df(z)}{dz}\right) dz + \int_{\frac{h_c}{2}}^{\frac{h_c}{2+h_t}} \mu_t(z) \left(\frac{df(z)}{dz}\right) dz$$

$$H_8 = \int_{-\frac{h_c}{2}-h_b}^{-\frac{h_c}{2}} \mu_b(z) z \left(\frac{df(z)}{dz}\right) dz + \int_{\frac{h_c}{2}}^{\frac{h_c}{2+h_t}} \mu_t(z) z \left(\frac{df(z)}{dz}\right) dz$$

$$H_9 = \int_{-\frac{h_c}{2}-h_b}^{-\frac{h_c}{2}} \mu_b(z) f(z) \left(\frac{df(z)}{dz}\right) dz + \int_{\frac{h_c}{2}}^{\frac{h_c}{2+h_t}} \mu_t(z) f(z) \left(\frac{df(z)}{dz}\right) dz$$

$$H_{10} = \int_{-\frac{h_c}{2}-h_b}^{-\frac{h_c}{2}} \mu_b(z) \left(\frac{df(z)}{dz}\right)^2 dz + \int_{\frac{h_c}{2}}^{\frac{h_c}{2+h_t}} \mu_t(z) \left(\frac{df(z)}{dz}\right)^2 dz$$

$$H_{11} = \int_{-\frac{h_c}{2}-h_b}^{-\frac{h_c}{2}} \mu_b(z) \left(\frac{d^2 f(z)}{dz^2}\right) dz + \int_{\frac{h_c}{2}}^{\frac{h_c}{2+h_t}} \mu_t(z) \left(\frac{d^2 f(z)}{dz^2}\right) dz$$

$$H_{12} = \int_{-\frac{h_c}{2}-h_b}^{-\frac{h_c}{2}} \mu_b(z) \left(\frac{d^2 f(z)}{dz^2}\right)^2 dz + \int_{\frac{h_c}{2}}^{\frac{h_c}{2+h_t}} \mu_t(z) \left(\frac{d^2 f(z)}{dz^2}\right)^2 dz$$

$$H_{13} = \int_{-\frac{h_c}{2}-h_b}^{-\frac{h_c}{2}} \mu_b(z) \left(\frac{df(z)}{dz}\right)\left(\frac{d^2 f(z)}{dz^2}\right) dz + \int_{\frac{h_c}{2}}^{\frac{h_c}{2+h_t}} \mu_t(z) \left(\frac{df(z)}{dz}\right)\left(\frac{d^2 f(z)}{dz^2}\right) dz$$

$$T_1 = \int_{-\frac{h_c}{2}}^{\frac{h_c}{2}} \mu_c(z) z^i dz, \qquad i = 0,1,2$$

$$T_4 = \int_{-\frac{h_c}{2}}^{\frac{h_c}{2}} \mu_c(z) f(z) dz, \qquad T_5 = \int_{-\frac{h_c}{2}}^{\frac{h_c}{2}} \mu_c(z) f^2(z) dz, \qquad T_6 = \int_{-\frac{h_c}{2}}^{\frac{h_c}{2}} \mu_c(z) z f(z) dz, \qquad T_7 = \int_{-\frac{h_c}{2}}^{\frac{h_c}{2}} \mu_c(z) \left(\frac{df(z)}{dz}\right) dz$$

$$T_8 = \int_{-\frac{h_c}{2}}^{\frac{h_c}{2}} \mu_c(z) z \left(\frac{df(z)}{dz}\right) dz, \qquad T_9 = \int_{-\frac{h_c}{2}}^{\frac{h_c}{2}} \mu_c(z) f(z) \left(\frac{df(z)}{dz}\right) dz, \qquad T_{10} = \int_{-\frac{h_c}{2}}^{\frac{h_c}{2}} \mu_c(z) \left(\frac{df(z)}{dz}\right)^2 dz$$

$$T_{11} = \int_{-\frac{h_c}{2}}^{\frac{h_c}{2}} \mu_c(z) \left(\frac{d^2 f(z)}{dz^2}\right) dz, \qquad T_{12} = \int_{-\frac{h_c}{2}}^{\frac{h_c}{2}} \mu_c(z) \left(\frac{d^2 f(z)}{dz^2}\right)^2 dz, \qquad T_{13} = \int_{-\frac{h_c}{2}}^{\frac{h_c}{2}} \mu_c(z) \left(\frac{df(z)}{dz}\right)\left(\frac{d^2 f(z)}{dz^2}\right) dz$$